JACS
JOURNAL OF THE AMERICAN CHEMICAL SOCIETY
Article
pubs.acs.org/JACS

Synthesis of 4H/*fcc* Noble Multimetallic Nanoribbons for Electrocatalytic Hydrogen Evolution Reaction

Zhanxi Fan,[†] Zhimin Luo,[†] Xiao Huang,[‡] Bing Li,[§] Ye Chen,[†] Jie Wang,[†] Yanling Hu,[†] and Hua Zhang*[,†]

[†]Center for Programmable Materials, School of Materials Science and Engineering, Nanyang Technological University, 50 Nanyang Avenue, 639798 Singapore

[‡]Key Laboratory of Flexible Electronics & Institute of Advanced Materials, Jiangsu National Synergistic Innovation Center for Advanced Materials, Nanjing Tech University, 30 South Puzhu Road, Nanjing 211816, PR China

[§]Institute of Materials Research and Engineering, Agency for Science, Technology and Research, 2 Fusionopolis Way, Innovis #08-03, 138634 Singapore

Supporting Information

ABSTRACT: Noble multimetallic nanomaterials, if only consisting of Au, Ag, Pt, and Pd, typically adopt the high-symmetry face-centered cubic (*fcc*) structure. Here for the first time, by using the 4H/*fcc* Au@Ag nanoribbons (NRBs) as seeds, we report the synthesis of 4H/*fcc* trimetallic Au@PdAg core–shell NRBs via the galvanic reaction method under ambient conditions. Moreover, this strategy can also be used to synthesize 4H/*fcc* trimetallic Au@PtAg and quatermetallic Au@PtPdAg core–shell NRBs. Impressively, for the first time, these alloy shells, i.e., PdAg, PtAg, and PtPdAg, epitaxially grown on the 4H/*fcc* Au core with novel 4H hexagonal phase were successfully synthesized. Remarkably, the obtained 4H/*fcc* Au@PdAg NRBs exhibit excellent electrocatalytic activity toward the hydrogen evolution reaction, which is even quite close to that of the commercial Pt black. We believe that our findings here may provide a novel strategy for the crystal-structure-controlled synthesis of advanced functional noble multimetallic nanomaterials with various promising applications.

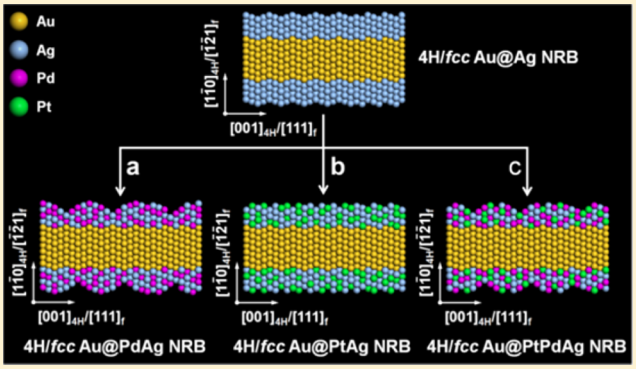

INTRODUCTION

Noble multimetallic nanomaterials with the number of metal elements $n \geq 3$ have attracted great research interest because of their superior physicochemical properties and stability, associated with the synergistic effect between multiple components,[1] as compared to those of their monometallic counterparts. In one promising application, noble multimetallic nanomaterials have been widely used for various heterogeneous catalytic reactions, e.g., organic reaction,[2] oxygen reduction reaction,[3] hydrogen evolution reaction (HER),[4] formic acid,[5] methanol,[6] and ethanol oxidation reactions.[7] It has been well-documented that the catalytic performances of noble multimetallic nanomaterials are largely affected by their size,[8] shape,[5a,9] composition,[5b,10] and architecture.[7,11] Importantly, recent studies confirmed that the crystal structures of noble multimetallic nanomaterials can significantly affect their catalytic properties.[1c,12] For instance, both catalytic activity and durability of FePtAu nanoparticles (NPs) toward the formic acid oxidation reaction can be significantly improved by transformation of the crystal phase from face-centered cubic (*fcc*) to face-centered tetragonal (*fct*) structures.[1c] Therefore, it is critically important to investigate the crystal-phase-controlled synthesis of noble multimetallic nanomaterials.

Normally, the crystal-phase control of noble multimetallic nanomaterials is mainly achieved under high temperature (usually ≥500 °C).[1c,12] As a typical example, Sun and co-workers found that the chemically ordered *fct* FePtAu NPs can be synthesized by annealing the as-prepared chemically disordered *fcc* FePtAu NPs at 600 °C under Ar/H_2 (v/v = 19/1) atmosphere.[1c] Such a high-temperature annealing method has also been used for the crystal structure transformation of trimetallic FePdPt and AuPdCo NPs from the disordered cubic alloy to ordered intermetallic structures.[12a,b] However, it still remains a challenge to realize the crystal-phase-controlled synthesis of noble multimetallic nanomaterials under mild experimental conditions. Until now, almost all of the reported noble multimetallic nanomaterials, if only consisting of Au, Ag, Pd, and Pt, adopt the common structure of *fcc*.[1b,6a,7,9,11,13]

Recently, our group first demonstrated the graphene oxide (GO)-templated synthesis of hexagonal close-packed (*hcp*, also known as the 2H phase) Au square sheets and the 4H hexagonal Au nanoribbons (NRBs).[14] Importantly, after noble metals, such as Ag, Pd, and Pt, coat on the aforementioned Au

Received: December 5, 2015
Published: January 10, 2016

DOI: 10.1021/jacs.5b12715
J. Am. Chem. Soc. 2016, 138, 1414–1419

nanostructures, a series of novel core−shell bimetallic nanomaterials has been synthesized, including the alternating 4H/*fcc* Au@Ag NRBs.[15] However, owing to the different reduction kinetics of noble metal precursors,[16] the direct synthesis of Au-based multimetallic NRBs is quite difficult and yet to be realized. In this contribution, for the first time we demonstrate the synthesis of alternating 4H/*fcc* Au@PdAg core−shell NRBs from 4H/*fcc* Au@Ag NRBs via a galvanic reaction method under ambient conditions. Moreover, 4H/*fcc* trimetallic Au@PtAg and quatermetallic Au@PtPdAg core−shell NRBs have also been prepared. Significantly, for the first time, 4H hexagonal structures of a series of noble metal alloys, i.e., PdAg, PtAg, and PtPdAg, are achieved, which epitaxially grow on the 4H/*fcc* Au core. As a proof-of-concept application, the obtained 4H/*fcc* Au@PdAg NRBs are used as a novel electrocatalyst for the HER and exhibit excellent catalytic performance close to that of commercial Pt black.

EXPERIMENTAL SECTION

Materials. Gold(III) chloride hydrate ($HAuCl_4{\cdot}xH_2O$, ∼50% Au basis), silver(I) nitrate ($AgNO_3$, ≥99.0%, ACS reagent), palladium(II) nitrate dihydrate ($Pd(NO_3)_2{\cdot}2H_2O$, ∼40% Pd basis), Nafion®117 solution (5 wt %, dispersed in a binary solvent of water and lower aliphatic alcohols), *n*-hexane ($CH_3(CH_2)_4CH_3$, technical-grade), potassium hydroxide (KOH, reagent-grade, 90%), and other chemical reagents used in this work without mention were all bought from Sigma-Aldrich (Saint Louis, Missouri, USA). Platinum(II) nitrate ($Pt(NO_3)_2$, ∼61% Pt basis) was purchased from Mateck GmbH (Jülich, Germany). Methanol (AR-grade, 99.99%) was purchased from Fisher Scientific (part of Thermo Fisher Scientific, Loughborough, UK). Ethanol (absolute, 99.9%) was purchased from Merck (Nordic European Centre, Singapore). Commercial Pd black (99.9%) and Pt black (99.99%) were purchased from Shanghai Hesen Electric Co., Ltd. (Shanghai, China). Milli-Q water obtained by using the Milli-Q Water Purification System (Millipore, Billerica, MA, USA) was used throughout the experiments. All of the chemical reagents were used as received without any further purification.

Synthesis of 4H/*fcc* Bimetallic Au@Ag Core−Shell NRBs. The starting material, i.e., 4H/*fcc* bimetallic Au@Ag NRBs, was synthesized on the basis of our previously reported approach with slight modification.[14b] In a typical experiment, 750 μL of $AgNO_3$ solution (100 mM, ethanol), 390 μL of oleylamine, 1.86 mL of hexane, and 3.0 mL of our previously reported 4H hexagonal Au NRB hexane solution[14b] were continuously added into a glass vial. After the glass vial was tightly sealed, it was heated using the water bath for 20 h at 58 °C. The obtained products were collected by centrifugation at 7000 rpm for 1 min, washed once with the mixture of ethanol and hexane (v/v = 1/1) and then four times with hexane, and finally redispersed into 3.0 mL of methanol or hexane.

Synthesis of 4H/*fcc* Trimetallic Au@PdAg Core−Shell NRBs. The 4H/*fcc* Au@PdAg NRBs were synthesized via the galvanic reaction between Ag in 4H/*fcc* Au@Ag bimetallic NRBs and Pd^{2+} ions. In a typical experiment, 300 μL of freshly prepared $Pd(NO_3)_2$ methanol solution (8 mM) was added into 3.0 mL of the obtained 4H/*fcc* bimetallic Au@Ag NRB methanol solution. The aforementioned mixture in a tightly sealed glass vial was ultrasonicated for 5 s and then kept undisturbed under ambient conditions for 10 min. The obtained products were collected by centrifugation (1 min, 7500 rpm), washed four times with methanol, and finally redispersed into methanol (3.0 mL).

Synthesis of Alternating 4H/*fcc* Trimetallic Au@PtAg Core−Shell NRBs. The alternating 4H/*fcc* Au@PtAg NRB was synthesized via the galvanic reaction between Ag in alternating 4H/*fcc* Au@Ag NRBs and Pt^{2+} ions. In a typical experiment, 500 μL of ethanol and 100 μL of freshly prepared $Pt(NO_3)_2$ solution (8 mM, ethanol) were, respectively, added into 500 μL of the obtained 4H/*fcc* Au@Ag NRB (dispersed in hexane). The aforementioned mixture in a tightly sealed glass bottle was ultrasonicated for 5 s, which was then kept undisturbed in a water bath for 1 h at 58 °C. The resulting products were collected by centrifugation at 7500 rpm for 1 min, washed twice with ethanol, and finally redispersed in 500 μL of ethanol.

Synthesis of 4H/*fcc* Quatermetallic Au@PtPdAg Core−Shell NRBs. The 4H/*fcc* quatermetallic Au@PtPdAg NRBs were synthesized via the galvanic reaction of Ag in 4H/*fcc* bimetallic Au@Ag NRBs with the mixture of Pt^{2+} and Pd^{2+} ions. In a typical experiment, after 50 μL of freshly prepared $Pt(NO_3)_2$ methanol solution (8 mM) and 50 μL of freshly prepared $Pd(NO_3)_2$ methanol solution (8 mM) were mixed, the aforementioned mixture was added into 1.0 mL of the obtained 4H/*fcc* bimetallic Au@Ag NRB methanol solution in a tightly sealed glass vial, which was sealed and ultrasonicated for 5 s and then kept undisturbed under ambient conditions for 10 min. The resulting product was collected by centrifugation at 7500 rpm for 1 min, washed twice with methanol, and finally redispersed in 1.0 mL of methanol.

Electrochemical Measurement. After the glassy carbon electrode (GCE) was consecutively polished by the α-Al_2O_3 powder with different sizes of particles, i.e., 1000, 300, and 50 nm, it was thoroughly ultrasonicated for 1 min in Milli-Q water and then ethanol. Then, 5.0 μL of catalyst solution, i.e., Au@PdAg NRBs in 0.06 wt % Nafion water solution (concentration of Pd = 0.50 mg/mL, measured by the inductive coupled plasma-optical emission spectroscopy), was dropped onto the surface of cleaned GCE. After drying under ambient conditions for 2 h, cyclic voltammetry (CV) and chronoamperometry were conducted in the three-electrode system on Autolab electrochemical workstation (PGSTAT12). Graphite rod, Ag/AgCl (KCl, 3 M), and the catalyst-modified GCE were used as counter, reference, and work electrodes, respectively. The electrocatalytic hydrogen evolution was measured by the linear sweep voltammetry (LSV) in H_2-saturated H_2SO_4 solution (0.5 M) at a scan rate of 5.0 mV/s. Electrocatalytic stability of catalyst was evaluated by the durable LSV cycling measurement.

In our measurements, the reference electrode was the Ag/AgCl electrode, which was carefully calibrated by using the reversible hydrogen electrode (RHE) in a highly pure H_2-saturated H_2SO_4 solution (0.5 M) with the Pt wire used as working electrode.[26] The CV curves were conducted at a scan rate of 1.0 mV/s. The average value of two potentials at a current density of zero was regarded as the thermodynamic potential for the electrocatalytic hydrogen electrode reaction (Figure S16). Therefore, the potential with respect to RHE in our experiments can be calculated as follows:

$$E(\mathrm{RHE}) = E(\mathrm{Ag/AgCl}) + 0.248\ \mathrm{V}$$

Characterization. All transmission electron microscopy (TEM) samples were prepared by dropping 5.0 μL of sample solutions onto the 200-mesh copper grids that are fully coated with carbon. After the TEM samples were dried under ambient conditions, the selected area electron diffraction (SAED) patterns, TEM, high-resolution TEM (HRTEM), and high-angle annular dark-field-STEM (HAADF-STEM) images, and the scanning TEM-energy dispersive X-ray spectroscopy (STEM-EDS) data were acquired on a transmission electron microscope (200 kV, JEOL JEM-2100F). The X-ray photoelectron spectroscopy (XPS) data were obtained by using the Theta Probe electron spectrometer (Thermo Scientific, ESCA-Lab-200i-XL).

RESULTS AND DISCUSSION

In a typical experiment, the alternating 4H/*fcc* bimetallic Au@Ag core−shell NRBs were synthesized according to our previously reported approach with a slight change (details in the Experimental Section).[14b] The typical TEM image and SAED pattern confirm the successful formation of Au@Ag core−shell NRBs with a unique alternating 4H/*fcc* structure (Figure S1), which is consistent with our previous result.[14b] An average Au/Ag atomic ratio of about 1.00/2.60 is obtained from STEM-EDS (Figure S2). The as-prepared 4H/*fcc* bimetallic Au@Ag NRBs were then used to synthesize 4H/*fcc* noble multimetallic NRBs, i.e., 4H/*fcc* Au@PdAg, Au@PtAg, and

DOI: 10.1021/jacs.5b12715
J. Am. Chem. Soc. 2016, 138, 1414−1419

Au@PtPdAg core−shell NRBs, via the galvanic reaction between Ag and noble metal precursors (Figure 1). Note that

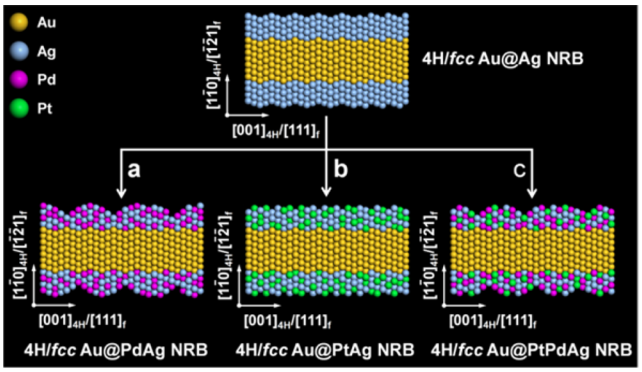

Figure 1. 4H/*fcc* Au@PdAg, Au@PtAg, and Au@PtPdAg core−shell NRBs were synthesized from 4H/*fcc* bimetallic Au@Ag core−shell NRBs via the galvanic reaction of Ag with (a) $Pd(NO_3)_2$, (b) $Pt(NO_3)_2$, and (c) a mixture of $Pt(NO_3)_2$ and $Pd(NO_3)_2$, respectively.

the galvanic reactions between Ag and $Pd(NO_3)_2$ or $Pt(NO_3)_2$ are thermodynamically favored because the standard reduction potentials of Pd^{2+} and Pt^{2+} ions are higher than that of an Ag^+ ion.[16,17]

As shown in the step a in Figure 1, trimetallic Au@PdAg core−shell NRBs were synthesized from the 4H/*fcc* bimetallic Au@Ag NRBs by the galvanic reaction between Ag and $Pd(NO_3)_2$ under ambient conditions (details in the Experimental Section). The XPS data confirmed the chemical states of Au(0), Ag(0) and Pd(0) in the obtained Au@PdAg NRBs (Figure S3). The composition of obtained Au@PdAg NRBs was investigated by STEM-EDS, which reveals an average Au/Ag/Pd atomic ratio of about 1.00/1.94/1.06 (Figure S4). A typical HAADF-STEM image and the corresponding STEM-EDS element mappings and line-scanning profile reveal that the PdAg alloy shell is formed on the Au core (Figures 2g−j and S5). Typical TEM images show that the Au@PdAg NRBs possess a rough dendritic surface (Figure 2a−c). The average thickness of the PdAg shell is approximately 5.0 nm. Interestingly, the SAED pattern of representative Au@PdAg NRBs demonstrates a $[110]_{4H}$-zone diffraction pattern along with many streaks in the close-packed direction of $[001]_{4H}$, indicating an intergrowth of *fcc* and 4H phases as well as twins and stacking faults along the directions of $[001]_{4H}/[111]_f$ (Figure 2d). No other randomly distributed diffraction spots are observed, suggesting that the PdAg shell is epitaxially grown on the Au core (Figure 2d). Note that the lattice mismatch between noble metals, such as Ag, Au, Pd, and Pt, is quite small (usually <5%) and thus favors their epitaxial growth between each other.[18] The typical HRTEM image clearly demonstrates coexistence of 4H and *fcc* structures in the obtained Au@PdAg NRBs (Figure 2e,f). Importantly, the lattice fringes coherently extend from the inside Au core to outside PdAg shell, further confirming the epitaxial relationship between the PdAg shell and Au core (Figure 2f), which is consistent with the electron diffraction result (Figure 2d). Likewise, a typical HRTEM image and the corresponding selected area fast Fourier transform (FFT) pattern confirm the successful formation of 4H hexagonal phase of the PdAg alloy shell (Figure 2f and Figure S6). Importantly, this is first report of the preparation of noble metal alloy nanostructures with a unique 4H hexagonal phase.

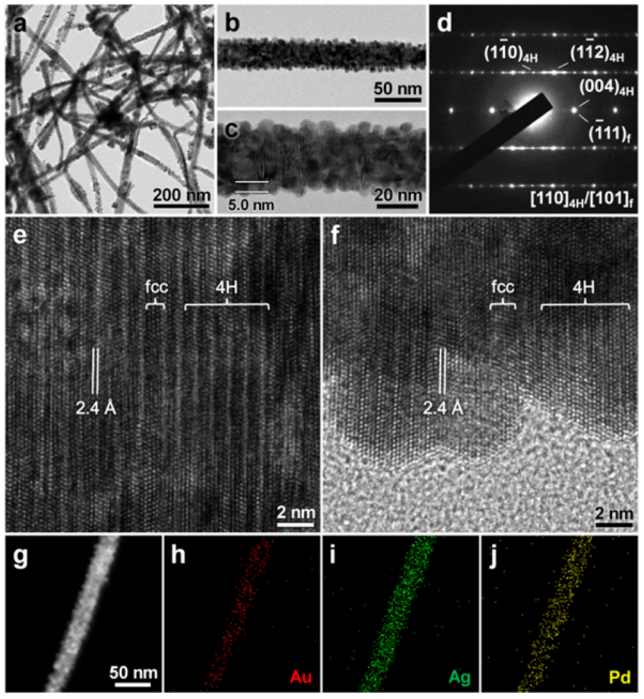

Figure 2. (a) Typical TEM image of 4H/*fcc* trimetallic Au@PdAg core−shell NRBs. (b and c) Magnified TEM images of a representative 4H/*fcc* Au@PdAg NRB. (d) Corresponding SAED pattern of a 4H/*fcc* trimetallic Au@PdAg NRB acquired from the zone axes of $[110]_{4H}/[101]_f$. (e and f) Typical HRTEM images of the obtained 4H/*fcc* trimetallic Au@PdAg NRBs collected from its center (e) and edge (f) areas. (g) Typical HAADF-STEM image and (h−j) STEM-EDS element mappings of a typical 4H/*fcc* trimetallic Au@PdAg NRB.

Notably, by simply changing the noble metal precursor from $Pd(NO_3)_2$ to $Pt(NO_3)_2$, trimetallic Au@PtAg core−shell NRBs were obtained from 4H/*fcc* bimetallic Au@Ag NRBs via the galvanic reaction at 58 °C (step b in Figure 1, details in the Experimental Section). Figure 3a−c shows the representative TEM images of obtained Au@PtAg NRBs. The average thickness of the PtAg shell is around 2.7 nm. The SAED pattern suggests that the Au@PtAg NRB crystallizes in the unique alternating 4H/*fcc* structures with some crystal defects such as twins and stacking faults (Figure 3d). No other randomly distributed diffraction spots are observed, indicating an epitaxial growth of the PtAg shell on Au core (Figure 3d). Typical HRTEM image of trimetallic Au@PtAg NRB demonstrates the intergrowth of *fcc* and 4H structures (Figure 3e). Importantly, the uncommon 4H hexagonal phase of the PtAg alloy shell was achieved, which has been further identified by the selected-area FFT pattern (Figure S7). The composition of Au@PtAg NRBs was measured by STEM-EDS, which reveals an average Au/Ag/Pt atomic ratio of about 1.00/0.58/0.23 (Figure S8). The uniform coating of PtAg alloy shell on the Au core is corroborated by the HAADF-STEM images and STEM-EDS element mappings and line scanning profile (Figures 3f−i and S9).

Significantly, via the simultaneous galvanic reaction of Ag with the mixture of $Pd(NO_3)_2$ and $Pt(NO_3)_2$, the quatermetallic Au@PtPdAg core−shell NRBs were also synthesized from 4H/*fcc* Au@Ag NRBs under ambient conditions (step c in Figure 1, details in the Experimental Section). Similar to the aforementioned trimetallic Au@PdAg NRBs (Figure 2a−c), the obtained quatermetallic Au@PtPdAg NRBs also have a

DOI: 10.1021/jacs.5b12715
J. Am. Chem. Soc. 2016, 138, 1414−1419

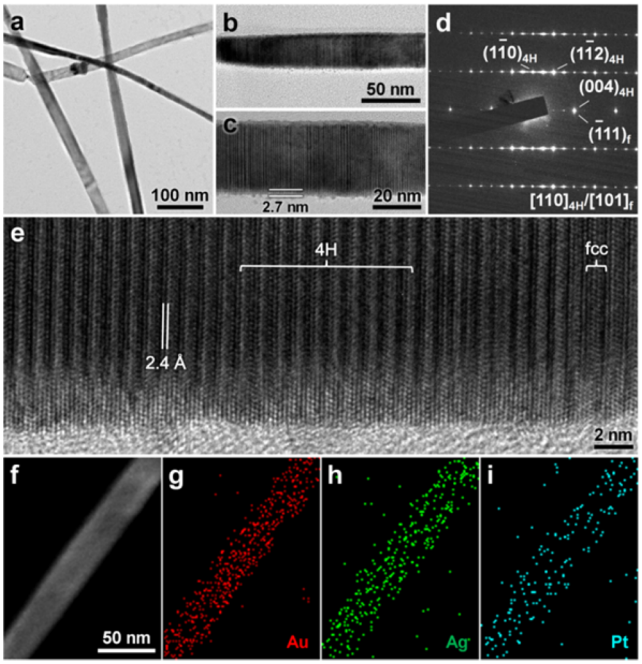

Figure 3. (a) Typical TEM image of 4H/*fcc* trimetallic Au@PtAg core−shell NRBs. (b and c) Magnified TEM images of a representative 4H/*fcc* trimetallic Au@PtAg NRB. (d) Corresponding SAED pattern of a 4H/*fcc* trimetallic Au@PtAg NRB acquired from the zone axes of $[110]_{4H}/[101]_f$. (e) Representative HRTEM image of the 4H/*fcc* trimetallic Au@PtAg NRB. (f) Typical HAADF-STEM image and (g−i) STEM-EDS element mappings of a typical 4H/*fcc* trimetallic Au@PtAg NRB.

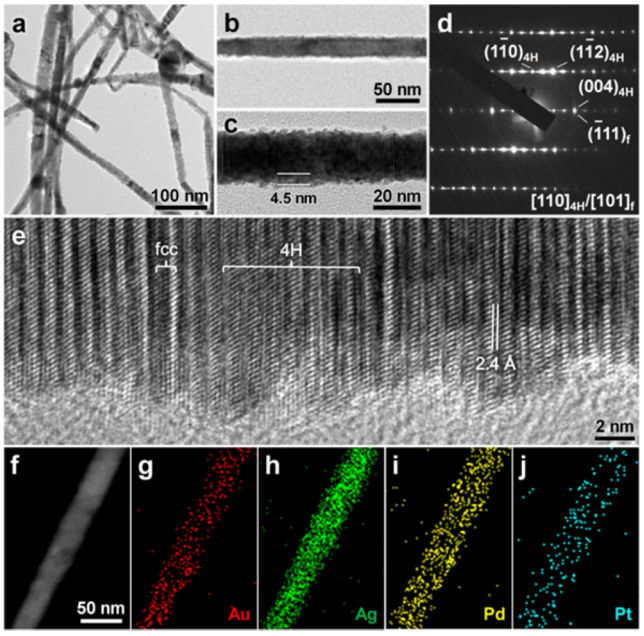

Figure 4. (a) Typical TEM image of 4H/*fcc* quatermetallic Au@PtPdAg core−shell NRBs. (b and c) Magnified TEM images of a representative 4H/*fcc* trimetallic Au@PtPdAg NRB. (d) Corresponding SAED pattern of a 4H/*fcc* trimetallic Au@PtPdAg NRB acquired from the zone axes of $[110]_{4H}/[101]_f$. (e) Representative HRTEM image of the obtained 4H/*fcc* trimetallic Au@PtPdAg NRBs. (f) Typical HAADF-STEM image and (g−j) STEM-EDS element mappings of a representative 4H/*fcc* trimetallic Au@PtPdAg NRB.

relatively rough surface (Figure 4a−c). The average thickness of PtPdAg shell is about 4.5 nm. The composition of Au@PtPdAg NRBs was characterized by STEM-EDS, which reveals an average Au/Ag/Pd/Pt atomic ratio of about 1.00/1.85/0.84/0.29 (Figure S10). Typical HAADF-STEM images, the corresponding STEM-EDS element mappings, and line-scanning profile reveal successful coating of the PtPdAg alloy shell on Au core (Figures 4f−j and S11). The representative SAED pattern of quatermetallic Au@PtPdAg NRBs shows a characteristic $[110]_{4H}$-zone pattern along with many streaks in the close-packed direction of $[001]_{4H}$, indicating an intergrowth of *fcc* and 4H phases as well as crystal defects such as twins and stacking faults along $[001]_{4H}/[111]_f$ directions (Figure 4d). Importantly, no other randomly distributed diffraction spots are observed, indicating that the PtPdAg alloy shell is epitaxially grown on the Au core (Figure 4d). The HRTEM image further confirms the alternating 4H/*fcc* structure of the obtained Au@PtPdAg NRBs and the epitaxial growth of the PtPdAg shell on Au core (Figure 4e). Moreover, the unique 4H hexagonal structure of PtPdAg alloy shell is also successfully obtained, which is further identified by the selected-area FFT pattern (Figure S12).

Recent studies have suggested that noble multimetallic nanomaterials are very promising catalysts used for electrocatalytic reduction of some small molecules, such as O_2[3] and H_2O[4]. As a proof-of-concept application, the obtained 4H/*fcc* Au@PdAg NRBs were used as a novel electrocatalyst for reduction of H_2O to H_2. Figure 5a demonstrates the representative polarization curve of electrodes modified with Au@PdAg NRBs, commercial Pd black, and Pt black, respectively. The Au@PdAg NRBs exhibit much higher electrocatalytic activity toward HER compared to that of Pd black, which is even comparable with that of Pt black. The onset potentials of Au@PdAg NRBs, commercial Pd black, and Pt black are 2.0, 85.0, and 0.5 mV, respectively (Figure 5b). Also, to achieve a current density of 10.0 mA/cm^2, the overpotentials for Au@PdAg NRBs and commercial Pd and Pt black are 26.2, 135.6, and 16.5 mV, respectively (Figure 5b). Note that both the onset potential and overpotential for Au@PdAg NRBs are quite close to those for the Pt black. Significantly, the Tafel slope of Au@PdAg NRBs was evaluated to be 30 mV/decade, which is much lower than that of Pd black (109 mV/decade measured in this work, which is close to 103 mV/decade reported previously)[19] and even very close to that of Pt black (27 mV/decade measured in this work, which is close to 29 mV/decade reported previously; Figure 5c)[20]. The low Tafel slope of Au@PdAg NRBs (i.e., 30 mV/decade) suggests that recombination of chemisorbed hydrogen atoms on their surface is the rate-limiting step and that the HER proceeds via the Volmer−Tafel mechanism.[21] Moreover, the electrocatalytic stability of Au@PdAg NRBs toward HER was also investigated. Remarkably, no obvious shift of the polarization curve is observed after 10 000 potential cycles from +0.448 to −0.152 V (vs RHE) in H_2SO_4 solution (0.5 M), indicating the high catalytic durability of Au@PdAg NRBs for the HER (Figure 5d). Impressively, there is no obvious change of shape and crystal structure of 4H/*fcc* Au@PdAg NRBs after 10 000 potential cycles, which was verified by TEM, HRTEM, and HAADF-STEM images, SAED pattern, and STEM-EDS element mappings (Figures S13 and S14), indicating that 4H/*fcc* Au@PdAg NRBs are quite stable toward the electrocatalytic HER.

DOI: 10.1021/jacs.5b12715
J. Am. Chem. Soc. 2016, 138, 1414−1419

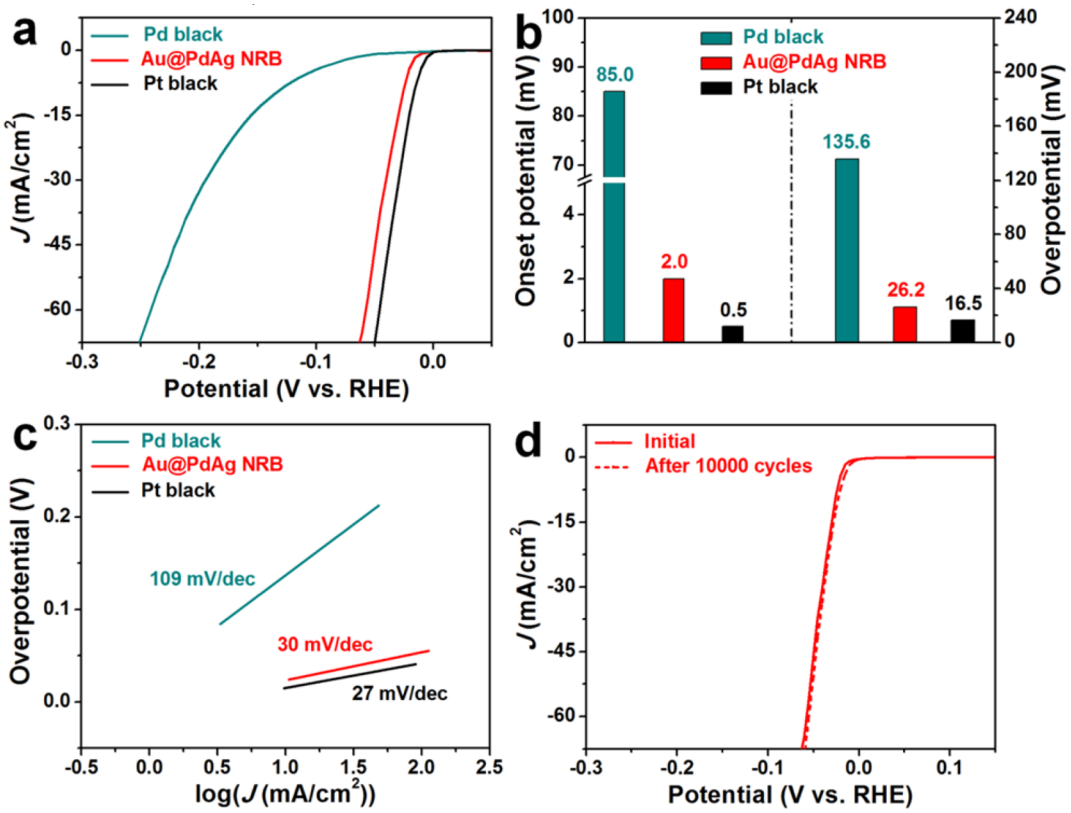

Figure 5. (a) Polarization curves of 4H/*fcc* trimetallic Au@PdAg NRBs, Pd black and Pt black. Linear sweep voltammetry was conducted in H_2SO_4 solution (0.5 M) at scan rate of 5.0 mV/s. The current density is denoted as "*J*". (b) Onset potentials and overpotentials (at current density of 10.0 mA/cm^2) of 4H/*fcc* trimetallic Au@PdAg NRBs, Pd black, and Pt black. (c) Corresponding Tafel plots for the data presented in panel a. (d) Durability test of 4H/*fcc* trimetallic Au@PdAg NRBs. The polarization curves were recorded before and after 10 000 potential cycles in H_2SO_4 solution (0.5 M) from +0.448 to −0.152 V (vs RHE).

The superior electrocatalytic performance of 4H/*fcc* Au@PdAg NRBs might arise from the interplay of their dendritic surface morphology,[18c] synergistic effect of their multiple components,[5b,10] and unique crystal structure.[1c,12] First, the dendritic growth of PdAg nanobranches on the Au core in Au@PdAg NRBs results in a very rough surface with rich atomic kinks and steps (Figure 2f), which are known as catalytically active sites for various chemical reactions.[18c,22] Second, recent studies revealed that the atomic vicinity of different metal atoms can change their electronic band structure via the electronic charge transfer between metal atoms, resulting in the enhancement of their catalytic activity.[5b,10,23] In this work, Pd and Ag are observed to form alloy nanostructures that epitaxially grown on the Au core in Au@PdAg NRBs (Figures 2d–j and S5), which could contribute to the catalytic activity of Au@PdAg NRBs via the synergistic effect among Au, Pd and Ag.[7,24] Third, previous experimental results have suggested that the catalytic performance of noble multimetallic nanomaterials can be significantly improved by rationally modulating their crystal structures.[1c,12] In this work, the Au@PdAg NRBs crystallize in an uncommon 4H/*fcc* crystal structure (Figure 2d–f), which might benefit the catalytic property of Au@PdAg NRBs toward the HER. In addition, electron transfer in the process of electrocatalytic reaction is relatively fast through the quasi-1D Au@PdAg NRBs that can act as direct pathway for the electron transport.[25] As expected, the electrochemical impedance spectroscopy measurement of Au@PdAg NRBs confirmed that their charge transfer resistance (16.2 Ω) is much smaller than that of Pd black (1410.2 Ω), but comparable with that of Pt black (11.5 Ω) (Figure S15).

CONCLUSIONS

For the first time, we have successfully synthesized a novel class of noble multimetallic nanomaterials, i.e., 4H/*fcc* Au@PdAg, Au@PtAg, and Au@PtPdAg core–shell NRBs, from the 4H/*fcc* bimetallic Au@Ag core–shell NRBs via the galvanic reaction method under mild conditions. Importantly, for the first time, the uncommon 4H hexagonal phases of a series of noble metal alloy nanostructures, i.e., PdAg, PtAg, and PtPdAg, are realized. Impressively, the obtained 4H/*fcc* Au@PdAg NRBs exhibit excellent electrocatalytic activity toward the HER, which is even quite close to that of commercial Pt black. Therefore, this novel nanomaterial holds great promise to replace the expensive Pt catalyst. It is believed that the rational crystal-phase-controlled synthesis of noble multimetallic nanomaterials will open up new opportunities for boosting their promising applications in various kinds of catalysis reactions.

ASSOCIATED CONTENT

Supporting Information

The Supporting Information is available free of charge on the ACS Publications website at DOI: 10.1021/jacs.5b12715.

HR-TEM, high- and low-magnification TEM, and HAADF-STEM images; FTT and SAED patterns; STEM-EDS and XPS spectra; STEM-EDS line scanning profiles; STEM-EDS elemental mappings; electrochem-

DOI: 10.1021/jacs.5b12715
J. Am. Chem. Soc. 2016, 138, 1414–1419

ical impedance spectroscopy data; and current−potential curve for the calibration of Ag/AgCl electrode. (PDF)

AUTHOR INFORMATION

Corresponding Author

*hzhang@ntu.edu.sg

Author Contributions

Z.F. and Z.L. made equal contributions to this work.

Notes

The authors declare no competing financial interest.

ACKNOWLEDGMENTS

This work was supported by Singapore MOE under the AcRF Tier 2 (ARC 19/15, No. MOE2014-T2-2-093; and ARC 26/13, No. MOE2013-T2-1-034) and the AcRF Tier 1 (RG5/13 and RGT18/13), and the Start-Up Grant (grant number: M4081296.070.500000) in NTU. This Research is also conducted by NTU-HUJ-BGU Nanomaterials for Energy and Water Management Programme under the Campus for Research Excellence and Technological Enterprise (CREATE), that is supported by the National Research Foundation, Prime Minister's Office, Singapore. X.H. is grateful for the financial support from the Natural Science Foundation of Jiangsu Province (BK20130927) and the National Natural Science Foundation of China (51322202).

REFERENCES

(1) (a) Huang, X.-Q.; Zhao, Z.-P.; Cao, L.; Chen, Y.; Zhu, E.-B.; Lin, Z.-Y.; Li, M.-F.; Yan, A.-M.; Zettl, A.; Wang, Y. M.; Duan, X.-F.; Mueller, T.; Huang, Y. *Science* **2015**, *348*, 1230. (b) Sasaki, K.; Naohara, H.; Choi, Y.-M.; Cai, Y.; Chen, W. F.; Liu, P.; Adzic, R. R. *Nat. Commun.* **2012**, *3*, 1115. (c) Zhang, S.; Guo, S.-J.; Zhu, H.-Y.; Su, D.; Sun, S.-H. *J. Am. Chem. Soc.* **2012**, *134*, 5060.

(2) Abazari, R.; Heshmatpour, F.; Balalaie, S. *ACS Catal.* **2013**, *3*, 139.

(3) (a) Liu, X. J.; Cui, C. H.; Li, H. H.; Lei, Y.; Zhuang, T. T.; Sun, M.; Arshad, M.-N.; Albar, H.-A.; Sobahi, T.-R.; Yu, S. H. *Chem. Sci.* **2015**, *6*, 3038. (b) Liu, S.-L.; Zhang, Q. H.; Li, Y.-F.; Han, M.; Gu, L.; Nan, C.-W.; Bao, J. C.; Dai, Z.-H. *J. Am. Chem. Soc.* **2015**, *137*, 2820. (c) Kang, Y.-J.; Snyder, J.; Chi, M.-F.; Li, D.-G.; More, K. L.; Markovic, N. M.; Stamenkovic, V. R. *Nano Lett.* **2014**, *14*, 6361.

(4) Cao, X.; Han, Y.; Gao, C.-Z.; Xu, Y.; Huang, X.-M.; Willander, M.; Wang, N. *Nano Energy* **2014**, *9*, 301.

(5) (a) Saleem, F.; Xu, B.; Ni, B.; Liu, H.-L.; Nosheen, F.; Li, H.-Y.; Wang, X. *Adv. Mater.* **2015**, *27*, 2013. (b) Scofield, M. E.; Koenigsmann, C.; Wang, L.; Liu, H.-Q.; Wong, S. S. *Energy Environ. Sci.* **2015**, *8*, 350.

(6) (a) Choi, B. S.; Lee, Y.-W.; Kang, S. W.; Hong, J.-W.; Kim, J.; Park, I.; Han, S.-W. *ACS Nano* **2012**, *6*, 5659. (b) Wu, Y.-E.; Wang, D.-S.; Zhou, G.; Yu, R.; Chen, C.; Li, Y.-D. *J. Am. Chem. Soc.* **2014**, *136*, 11594.

(7) Shi, Q. R.; Zhang, P.-N.; Li, Y. J.; Xia, H.-B.; Wang, D. Y.; Tao, X.-T. *Chem. Sci.* **2015**, *6*, 4350.

(8) Guo, S. J.; Zhang, S.; Su, D.; Sun, S.-H. *J. Am. Chem. Soc.* **2013**, *135*, 13879.

(9) Kang, S. W.; Lee, Y.-W.; Park, Y.; Choi, B. S.; Hong, J.-W.; Park, K. H.; Han, S.-W. *ACS Nano* **2013**, *7*, 7945.

(10) Wang, D. Y.; Chou, H.-L.; Lin, Y. C.; Lai, F.-J.; Chen, C. H.; Lee, J.-F.; Hwang, B. J.; Chen, C. C. *J. Am. Chem. Soc.* **2012**, *134*, 10011.

(11) Xie, X. B.; Gao, G.-H.; Kang, S.-D.; Shibayama, T.; Lei, Y.-H.; Gao, D. Y.; Cai, L.-T. *Adv. Mater.* **2015**, *27*, 5573.

(12) (a) Ghosh, T.; Vukmirovic, M. B.; DiSalvo, F.-J.; Adzic, R.-R. *J. Am. Chem. Soc.* **2010**, *132*, 906. (b) Kuttiyiel, K.-A.; Sasaki, K.; Su, D.; Wu, L.-J.; Zhu, Y. M.; Adzic, R.-R. *Nat. Commun.* **2014**, *5*, 5185. (c) Fan, Z. X.; Zhang, H. *Chem. Soc. Rev.* **2016**, *45*, 63.

(13) Wang, L.; Yamauchi, Y. *J. Am. Chem. Soc.* **2010**, *132*, 13636.

(14) (a) Huang, X.; Li, S.; Huang, Y. Z.; Wu, S.-X.; Zhou, X.; Li, S.; Gan, C. L.; Boey, F.; Mirkin, C. A.; Zhang, H. *Nat. Commun.* **2011**, *2*, 292. (b) Fan, Z. X.; Bosman, M.; Huang, X.; Huang, D.; Yu, Y.; Ong, K. P.; Akimov, Y. A.; Wu, L.; Li, B.; Wu, J.; Huang, Y.; Liu, Q.; Eng Png, C.; Lip Gan, C.-L.; Yang, P.-D.; Zhang, H. *Nat. Commun.* **2015**, *6*, 7684.

(15) (a) Fan, Z. X.; Huang, X.; Han, Y.; Bosman, M.; Wang, Q.-X.; Zhu, Y.-H.; Liu, Q.; Li, B.; Zeng, Z.-Y.; Wu, J.; Shi, W. X.; Li, S. Z.; Gan, C. L.; Zhang, H. *Nat. Commun.* **2015**, *6*, 6571. (b) Fan, Z. X.; Zhu, Y. H.; Huang, X.; Han, Y.; Wang, Q. X.; Liu, Q.; Huang, Y.; Gan, C. L.; Zhang, H. *Angew. Chem., Int. Ed.* **2015**, *54*, 5672.

(16) Xia, X. H.; Wang, Y.; Ruditskiy, A.; Xia, Y.-N. *Adv. Mater.* **2013**, *25*, 6313.

(17) (a) Chen, J.-Y.; Wiley, B.; McLellan, J.; Xiong, Y.-J.; Li, Z.-Y.; Xia, Y.-N. *Nano Lett.* **2005**, *5*, 2058. (b) González, E.; Arbiol, J.; Puntes, V. F. *Science* **2011**, *334*, 1377.

(18) (a) Fan, F.-R.; Liu, D. Y.; Wu, Y.-F.; Duan, S.; Xie, Z. X.; Jiang, Z.-Y.; Tian, Z. Q. *J. Am. Chem. Soc.* **2008**, *130*, 6949. (b) Habas, S. E.; Lee, H.; Radmilovic, V.; Somorjai, G.-A.; Yang, P.-D. *Nat. Mater.* **2007**, *6*, 692. (c) Lim, B.; Jiang, M.-J.; Camargo, P.-H. C.; Cho, E.-C.; Tao, J.; Lu, X.-M.; Zhu, Y. M.; Xia, Y.-N. *Science* **2009**, *324*, 1302. (d) Wu, J. B.; Gao, W.-P.; Wen, J. G.; Miller, D.-J.; Lu, P.; Zuo, J. M.; Yang, H. *Nano Lett.* **2015**, *15*, 2711.

(19) Pentland, N.; Bockris, J. O. M.; Sheldon, E. *J. Electrochem. Soc.* **1957**, *104*, 182.

(20) Conway, B.-E.; Bockris, J. O. M. *J. Chem. Phys.* **1957**, *26*, 532.

(21) Conway, B. E.; Tilak, B.-V. *Electrochim. Acta* **2002**, *47*, 3571.

(22) (a) Fujita, T.; Guan, P.-F.; McKenna, K.; Lang, X. Y.; Hirata, A.; Zhang, L.; Tokunaga, T.; Arai, S.; Yamamoto, Y.; Tanaka, N.; Ishikawa, Y.; Asao, N.; Yamamoto, Y.; Erlebacher, J.; Chen, M.-W. *Nat. Mater.* **2012**, *11*, 775. (b) Tian, N.; Zhou, Z. Y.; Sun, S. G.; Ding, Y.; Wang, Z.-L. *Science* **2007**, *316*, 732.

(23) Strasser, P.; Koh, S.; Anniyev, T.; Greeley, J.; More, K.; Yu, C. F.; Liu, Z.-C.; Kaya, S.; Nordlund, D.; Ogasawara, H.; Toney, M. F.; Nilsson, A. *Nat. Chem.* **2010**, *2*, 454.

(24) Coulthard, I.; Sham, T. K. *Phys. Rev. Lett.* **1996**, *77*, 4824.

(25) Xia, Y.-N.; Yang, P. D.; Sun, Y.-G.; Wu, Y. Y.; Mayers, B.; Gates, B.; Yin, Y.-D.; Kim, F.; Yan, H. *Adv. Mater.* **2003**, *15*, 353.

(26) (a) Liang, Y.-Y.; Li, Y. G.; Wang, H.-L.; Zhou, J. G.; Wang, J.; Regier, T.; Dai, H.-J. *Nat. Mater.* **2011**, *10*, 780. (b) Deng, J.; Ren, P. J.; Deng, D. H.; Yu, L.; Yang, F.; Bao, X.-H. *Energy Environ. Sci.* **2014**, *7*, 1919.

DOI: 10.1021/jacs.5b12715
J. Am. Chem. Soc. 2016, 138, 1414−1419